Low-Frequency (1/*f*) Noise in Nanocrystal Field-Effect Transistors

Yuming Lai,[†] Haipeng Li,[†] David K. Kim,[‡] Benjamin T. Diroll,[§] Christopher B. Murray,[‡,§] and Cherie R. Kagan*[,†,‡,§]

[†]Department of Electrical and Systems Engineering, [‡]Department of Materials Science and Engineering, and [§]Department of Chemistry, University of Pennsylvania, Philadelphia, Pennsylvania 19104, United States

ABSTRACT We investigate the origins and magnitude of low-frequency noise in high-mobility nanocrystal field-effect transistors and show the noise is of 1/*f*-type. Sub-band gap states, in particular, those introduced by nanocrystal surfaces, have a significant influence on the 1/*f* noise. By engineering the device geometry and passivating nanocrystal surfaces, we show that in the linear and saturation regimes the 1/*f* noise obeys Hooge's model of mobility fluctuations, consistent with transport of a high density of accumulated carriers in extended electronic states of the NC thin films. In the subthreshold regime, the Fermi energy moves deeper into the mobility gap and sub-band gap trap states give rise to a transition to noise dominated by carrier number fluctuations as described in McWhorter's model. CdSe nanocrystal field-effect transistors have a Hooge parameter of 3×10^{-2}, comparable to other solution-deposited, thin-film devices, promising high-performance, low-cost, low-noise integrated circuitry.

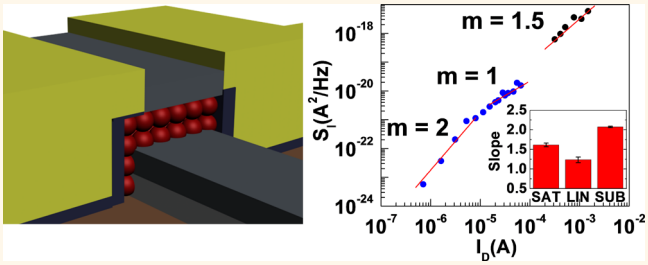

KEYWORDS: CdSe · nanocrystals · 1/*f* noise · low-frequency noise · field-effect transistors · trap states · charge transport

Colloidal semiconductor nanocrystals (NCs) are of great interest due to their size and shape-tunable optical and electronic properties.[1−3] As colloids, NC dispersions are akin to inks, allowing low-cost, solution-based deposition of large-area, thin-film devices, even on flexible substrates.[4−8] Successive breakthroughs in enhancing NC thin-film conductivities have led to demonstrations of nanocrystal field-effect transistors (NCFETs) with mobilities >15 cm^2/Vs[9−11] and their integration into flexible analog and digital circuits.[12] Optimization of NC thin-film carrier lifetime and mobility has given rise to NC solar cells with power conversion efficiencies of >4%[13−15] and to photodetectors with detectivities of $>10^{10}$ Jones.[11,16,17] However, applications of these promising devices and circuits require an understanding of noise, that is, the random fluctuations that occur in their electrical signals, particularly at the low frequencies where these devices operate. Measurements of NC thin-film photodetectors have shown that noise limits detectivity.[16,18]

Flicker noise (also known as 1/*f* noise) is often dominant at $f < 100$ kHz in nearly all electronic devices. In integrated circuits, flicker noise is known to reduce the noise margin and lead to unstable circuits.[19] The 1/*f* noise, while undesirable for device applications, also has developed into a field of interest to probe the mechanisms of charge transport in electronic materials.[20−23] The 1/*f* noise in electronic materials is commonly explored in the geometry of the field-effect transistor. Two models have been proposed to explain the origin of the noise. Flicker noise arises from current fluctuations, $\Delta I \propto qN(\Delta\mu) + q(\Delta N)\mu$, dominated by carrier mobility fluctuations ($\Delta\mu$) in the Hooge model[24] or carrier number fluctuations (ΔN) in the McWhorter model.[25] The magnitude and frequency dependence of the noise generated by these current fluctuations are described by the noise spectral density. In the Hooge model, mobility fluctuations arise from scattering between carriers and phonons or impurities.[26,27] The noise spectral density expression[28] depends on the device operation mode. In the transistor's linear regime, the noise spectral density is described by

$$S_I(f) = \frac{q\mu}{L^2}\frac{\alpha_H}{f} I_D V_{DS} \qquad (1)$$

* Address correspondence to kagan@seas.upenn.edu.

Received for review August 1, 2014 and accepted September 7, 2014.

Published online September 07, 2014
10.1021/nn504303b

and in the saturation regime by

$$S_I(f) = \frac{\alpha_H}{f} q\sqrt{2} \frac{\mu^{1/2}}{W^{1/2}L^{3/2}C_{ox}^{1/2}} I_D^{3/2} \quad (2)$$

where μ is the carrier mobility, α_H is the Hooge parameter, W and L are the device channel width and length, C_{ox} is the oxide unit capacitance, and I_D is the device drain−source current. In the McWhorter model, it is believed that traps inside the gate oxide layer of the transistor serve as centers for trapping−detrapping and lead to the carrier number fluctuations that appear as 1/*f* noise. The noise spectral density is given by

$$S_I(f) \frac{q^4}{kT} \frac{N_T}{WLf\gamma C_{ox}} \frac{1}{\eta^2} I_D^2 \quad (3)$$

where N_T is the trap density of states (eV^{-1} cm^{-3}) near the Fermi energy, γ is the tunneling parameter of traps ($\gamma = 1/\lambda, \lambda = 0.1$ nm), and η is related to the subthreshold swing S defined as $\eta = (qS)/((\ln 10)kT)$ and $S = (\partial V_{GS})/(\partial(\log_{10} I_D))$. This model has been extended to include traps that originate from imperfections in the semiconductor layer, either from bulk defects or from grain boundaries in amorphous and polycrystalline materials.[29−31] Both Hooge and McWhorter models have been extensively applied to conventional Si and III−V FETs[32−34] and recently have been used to describe noise in transistors constructed from novel semiconductor materials, such as organic semiconductors,[35−37] graphene,[38−40] carbon nanotubes,[41,42] and nanowires.[43,44] Nonetheless, the theory of 1/*f* noise still engenders great debate.

Here we report a systematic study of the low-frequency noise in CdSe NCFETs and show that the noise has 1/*f* behavior. We compare device performance and 1/*f* noise amplitude from devices with top-contact (TC) and bottom-contact (BC) geometries. The noise in BC NCFETs is governed by the source−drain to NC thin-film contacts, whereas in TC NCFETs, noise arises from the NC channel, giving us a platform to study and correlate noise spectral density and charge transport mechanisms in NC thin films. We show that 1/*f* noise relates to NC thin-film electronic structure, where the McWhorter model describes 1/*f* noise in the subthreshold regime and the Hooge model describes 1/*f* noise in the device linear and saturation regimes. The noise is described by a Hooge parameter of 3×10^{-2}, comparable to what has been reported in polycrystalline CdSe,[45] solution-deposited organic semicondutor,[37] and amorphous InGaZnO thin-film transistors,[46] and is within 1 order of magnitude of that for amorphous Si transistors.[32]

RESULTS AND DISCUSSION

Figure 1A,B shows device output characteristics, and Supporting Information Figure S1A compares device transfer characteristics for TC and BC NCFETs. Higher current levels are seen above the threshold in the TC devices as the field-effect mobility for electrons in TC devices is higher than that in BC devices (Table 1 and Supporting Information discussion). To study the origin of the performance difference, the trap density at the semiconductor/gate dielectric interface and the device

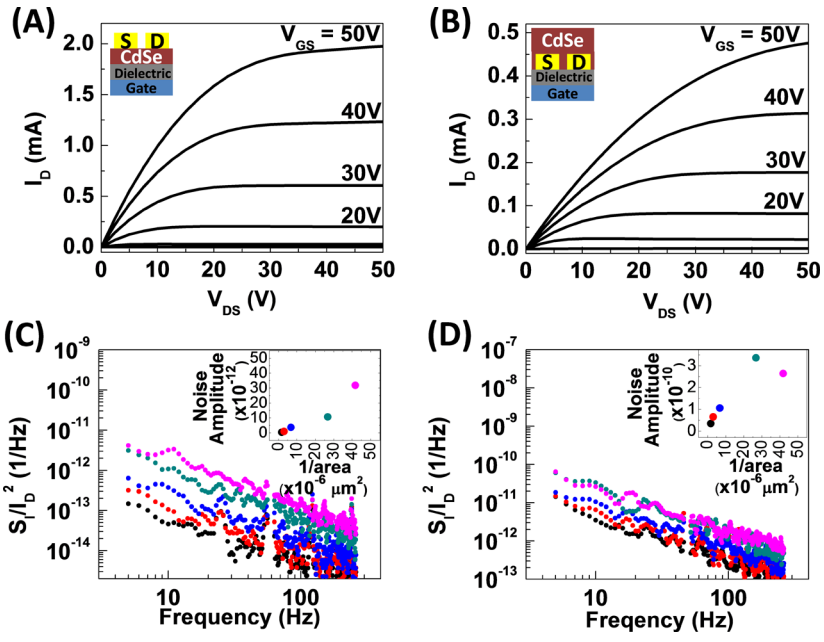

Figure 1. Device output characteristics (I_D-V_{DS}) for (A) top-contact and (B) bottom-contact CdSe NCFETs. Normalized drain current spectral density (S_I/I_D^2) *vs* frequency for (C) top-contact and (D) bottom-contact CdSe NCFETs, where the channel width over length ratio (W/L) is 15 for all devices and the length is (magenta) 40 μm, (green) 50 μm, (blue) 100 μm, (red) 150 μm, and (black) 200 μm. Insets in (A) and (B) are schematics of the top-contact and bottom-contact NCFETs, respectively. Insets in (C) and (D) show the relationship between noise amplitude and device area for a representative frequency of 10 Hz.

TABLE 1. Device Resistances Extracted Using the Transmission Line Method and Carrier Mobilities for TC and BC Devices[a]

	V_{GS} = 50 V					
	top contact			bottom contact		
channel length (μm)	R_{total} (Ω)	$R_{contact}/W$ (Ω)	mobility (cm^2/Vs)	$R_{contact}$ (Ω)	$R_{contact}/W$ (Ω)	mobility (cm^2/Vs)
30	8.8×10^3	-2.1×10^3	25.0	7.7×10^4	5.9×10^4	2.26
40	9.4×10^3	-1.6×10^3	24.5	6.2×10^4	4.4×10^4	2.69
50	9.7×10^3	-1.3×10^3	22.9	5.3×10^4	3.6×10^4	3.11
100	1.0×10^4	-6.5×10^2	20.7			
150	1.0×10^4	-4.3×10^2	19.9	2.9×10^4	1.2×10^4	6.95
200				2.6×10^4	8.9×10^3	9.38

[a] All data shown are at V_{GS} = 50 V. Note: Only saturation regime mobilities are presented in this table, as mobility for NCFETs is weakly dependent on V_{DS}.[9]

resistances are analyzed. The trap density at the semiconductor/gate dielectric interface can be derived from the subthreshold swing

$$S = \frac{kT}{q} \times \ln 10 \times \left(1 + \frac{qN_{it}}{C_{ox}}\right) \quad (4)$$

where N_{it} is the interface trap density (cm^{-2}).[47] The subthreshold slope for TC and BC devices is nearly identical, as expected given that both devices present the same CdSe NC/Al_2O_3 interface and therefore have a similar calculated average interface trap density over several devices of $5.0 \pm 1.8 \times 10^{12}$ cm^{-2} for TC and $5.5 \pm 0.5 \times 10^{12}$ cm^{-2} for BC configurations. Using the output characteristics in the linear regime, we calculate the contact resistance according to the transmission line method [$R_{total} \times W = R_{contact} + R_{channel} \times L$]. Supporting Information Figure S1B,C shows the total device resistance (R_{total}) as a function of channel length for different gate voltages (V_{GS}) that is used to extrapolate the contact resistance ($R_{contact}$), assuming a uniform channel resistance ($R_{channel}$). The results are summarized for V_{GS} = 50 V in (Table 1). It is evident that the BC devices suffer from large contact resistance, as high as 77% of the total resistance in L = 30 μm devices. Contact resistance distinctly influences the field-effect mobility of BC devices, such that high contact resistances at shorter channel lengths reduce the effective device mobility. For TC devices, $R_{channel}$ is dominant over the $R_{contact}$ (Table 1 and Supporting Information Table S1). In fact, we find negative values of $R_{contact}$, which we believe is an artifact arising from the assumption of uniform $R_{channel}$ adopted in transmission line method. A slight trend of increased mobility for shorter channel devices is observed, which we attribute to nonuniformities in indium diffusion and doping as the channel length increases.[9]

Figure 1C,D shows representative normalized drain current spectral density (S_I/I_D^2) *versus* frequency characteristics for varying channel length TC and BC devices, respectively, measured in the saturation regime (V_{DS} = 50 V, V_{GS} = 50 V). The low-frequency noise displays typical 1/f dependence and clearly shows that BC devices have higher noise than TC devices at each equivalent channel length. Noise amplitude (A), defined as $S(f) = S_I(f)/I_D^2 = A/f$, scales linearly with device channel area for both TC and BC device configurations (Figure 1C,D inset), consistent with previous reports that noise is inversely proportional to carrier number.[32,48]

Since $R_{contact}$ is extracted from linear regime device characteristics, we compare S_I/I_D^2 measured in the saturation (V_{DS} = 50 V, V_{GS} = 50 V) to that in the linear regime (V_{DS} = 5 V, V_{GS} = 50 V). Supporting Information Figure S1D shows that the noise is similar in the linear and saturation regimes at V_{GS} = 50 V, suggesting that the noise is weakly dependent on V_{DS}. To validate this, noise is assumed to be the sum of two uncorrelated noise sources, one from the channel and the other from the contacts, and is expressed as follows

$$S = \frac{S_I}{I_D^2} = \frac{S_{R_{total}}}{R_{total}^2} = \frac{S_{R_{channel}} + S_{R_{contact}}}{(R_{channel} + R_{contact})^2} \quad (5)$$

where $S_{R_{channel}}$ and $S_{R_{contact}}$ are the noises from the channel and contact regions and $R_{channel}$ and $R_{contact}$ are the channel and contact resistances, as described above.[32,49] These four components depend on W and L. We derive the dependence of S_I/I_D^2 on L (Supporting Information discussion) for different magnitudes of the noise and resistance sources and summarize the results in Table 2 for both constant W/L and constant W devices. We compare the L dependence of S_I/I_D^2 for constant W/L TC and BC devices in Figure 2A. The result differentiates the dominant noise sources in TC and BC devices, as TC devices follow an L^{-2} dependence, consistent with channel noise and resistance dominating over the contributions from the contacts, whereas for BC devices the L^{-1} relationship supports the dominance of the contact regions to the noise. The use of the length dependence of the noise to distinguish the noise contributions from channel and contact regions has been previously applied to studies of organic thin-film transistors.[35,50] However, in the literature, constant W is commonly derived and used and not constant W/L. In order to verify our derivation in Table 2, we prepare TC devices where constant W/L and constant

W are both included on the same sample. Indeed, in Figure 2B, TC devices show L^{-1} for constant W and L^{-2} for constant W/L (statistics are shown in Supporting Information Figure S2) as the channel region is the major source of noise in this device configuration. As BC devices suffer from additional $1/f$ noise originating from high-resistance metal-to-semiconductor contacts, only TC devices are used as a platform to study the $1/f$ noise characteristics arising from the NC thin-film channel.

The gate voltage dependence of the $1/f$ noise has been widely used to examine the origin of the low-frequency noise and relate the noise to mechanisms of charge transport in materials systems.[32,49,51] To collect the gate-voltage-dependent $1/f$ noise characteristics, devices are under constant voltage stress for an accumulated time of ~25 min. Bias stress in thin-film transistors commonly leads to I_D that varies over time.[52−54] We observe bias stress effects in our TC devices when operated in both saturation (Supporting Information Figure S3A) and linear (Supporting Information Figure S3B) regimes, leading to an abrupt current drop at the onset of stress that gradually becomes more stable after a few seconds. For each stress bias, I_D is therefore based on averaging the current from 10 s to the end of the voltage stress (Supporting Information Figure S4, blue stars). The observed decay in I_D arises from a shift of the device characteristics toward increased threshold voltage (V_T) (Supporting Information Figure S4A). These stress effects are more severe at lower V_{GS}, making the determination of I_D and device operation mode more difficult. Note the effects of bias stress are small in the noise measurements collected at a single high V_{GS} values, as in Figure 1C,D.

We find that we can dramatically reduce bias stress effects in TC devices by encapsulating the devices with an atomic layer deposition (ALD)-grown Al_2O_3 layer. ALD oxides have been previously reported to reduce device hysteresis in NCFETs.[5,54] Supporting Information Figure S3A,B shows the greater stability of encapsulated TC devices in the saturation and linear regimes, respectively. I_D remains at 80% of the initial current in encapsulated devices, as opposed to 40% or lower for devices without encapsulation after 25 min of accumulated stress. The time dependence of I_D fits well to a stretched exponential function, which is commonly used to describe bias stress effects in devices (Supporting Information Figure S5 and Supporting Information discussion). Upon encapsulation, the device hysteresis is also smaller (Supporting Information Figure S4B), with nearly no shift in device characteristics before and after noise measurement. Notably, the average stress current matches the device characteristics in saturation, linear, and subthreshold regions. This additional Al_2O_3 encapsulation layer minimizes device uncertainties and provides stable devices for gate-voltage-dependent $1/f$ noise measurements.

Figure 3A,B displays the drain current spectral density (S_I) *versus* frequency for Al_2O_3-encapsulated TC devices as a function of V_{GS}, at V_{DS} = 1 V, capturing

TABLE 2. Length-Dependent Normalized Drain Current Spectral Density Relationship for W/L= Constant and W = Constant

$$S_I(f)/I_D^2 = S_{R\text{total}}(f)/R_{\text{total}}^2 = S_{R\text{channel}} + S_{R\text{contact}}/(R_{\text{channel}} + R_{\text{contact}})^2$$

	W/L = const.	W = const.
$R_{\text{channel}} > R_{\text{contact}}$ $S_{R\text{channel}} > S_{R\text{contact}}$	$\propto 1/L^2$	$\propto 1/L$
$R_{\text{channel}} > R_{\text{contact}}$ $S_{R\text{contact}} > S_{R\text{channel}}$	$\propto 1/L$	$\propto 1/L^2$
$R_{\text{contact}} > R_{\text{channel}}$ $S_{R\text{channel}} > S_{R\text{contact}}$	const.	$\propto L$
$R_{\text{contact}} > R_{\text{channel}}$ $S_{R\text{contact}} > S_{R\text{channel}}$	$\propto L$	const.

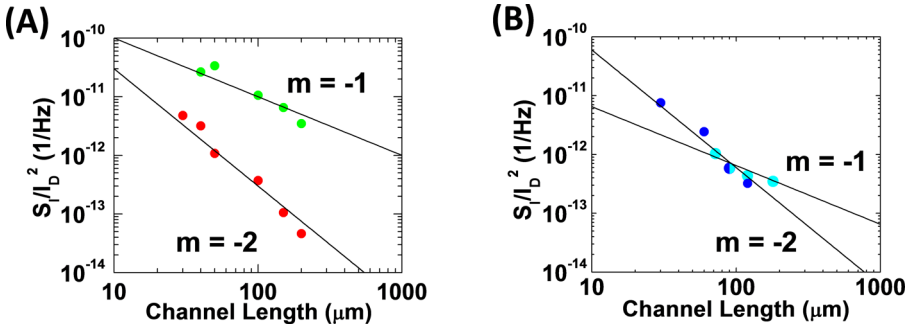

Figure 2. Normalized drain current spectral density (S_I/I_D^2) as a function of channel length varying from 30 to 200 μm, collected at a fixed frequency of 10 Hz, V_{DS} = 50 V and V_{GS} = 50 V. (A) Representative channel length dependence of S_I/I_D^2 for top-contact (red) and bottom-contact (green) devices with a constant W/L of 15. (B) Channel length dependence of S_I/I_D^2 for top-contact devices with constant W/L (blue) and fixed channel width of 1800 μm (cyan). Note: The device channel length of 90 μm and channel width of 1800 μm are common, representing the constant W/L ratio of 20 and the constant channel width of 1800 μm. Slopes of $m = -1$ and $m = -2$ lines are shown for reference.

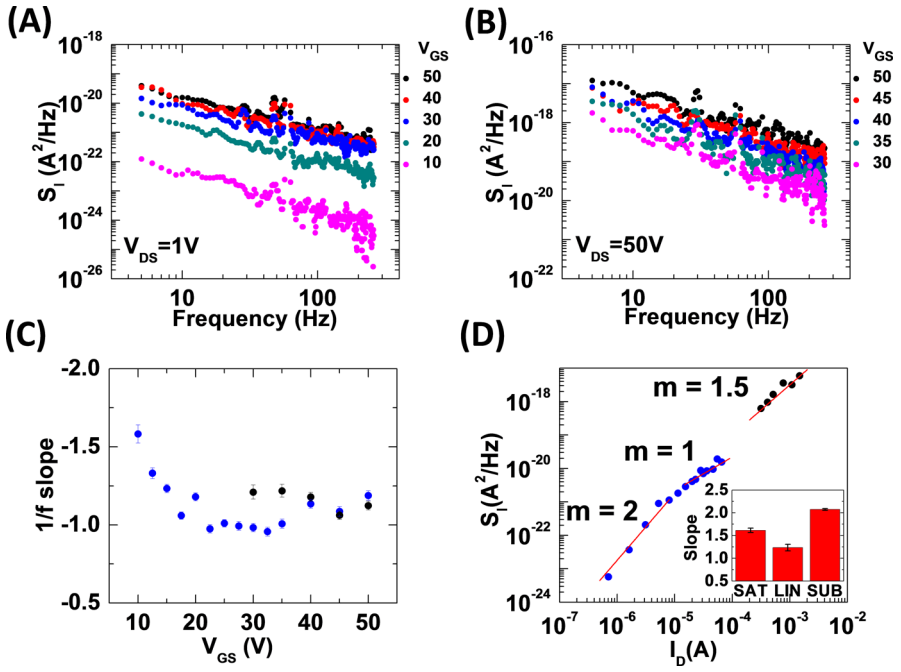

Figure 3. Spectral current density (S_I) of Al_2O_3-encapsulated, top-contact devices as a function of frequency measured at (A) V_{DS} = 1 V and (B) V_{DS} = 50 V under various V_{GS} values. (C) Slope fit of 1/*f* from S_I *vs* frequency as a function of V_{GS} at V_{DS} = 1 V (blue) and V_{DS} = 50 V (black). (D) S_I *vs* I_D at a frequency of 10 Hz for devices biased in saturation at V_{DS} = 50 V (black) and linear and subthreshold regimes at V_{DS} = 1 V (blue). Slopes (*m*) of 1, 1.5, and 2 are drawn for reference. Inset: Statistics from four devices of the slope of S_I *vs* I_D, measured in the saturation, linear, and subthreshold regimes, respectively.

device operation in the linear and subthreshold regimes (V_T is ~15 V), and at V_{DS} = 50 V, showing operation in the saturation mode. Although 1/*f* behavior is observed, the frequency exponent (γ in f^{γ}) is not a constant value of −1. Figure 3C depicts the frequency exponent for saturation (V_{DS} = 50 V, black) and linear to subthreshold (V_{DS} = 1 V, blue) regimes as a function of V_{GS}. For V_{DS} = 50 V, γ changes from −1 to more negative values with decreasing V_{GS}, whereas for V_{DS} = 1 V, γ is nearly constant at −1 for a wide range of V_{GS} values and then abruptly changes to more negative values as the device transitions from the linear to subthreshold regimes. Our observations for the noise behavior in NCFETs are consistent with the deviation of γ from −1 reported for semiconductors with a density of trap states in the band gap and are related to the position of the Fermi energy (E_F) as it is shifted through the density of states in different bias regimes.[30,55]

Another way to view these data is by plotting S_I *versus* I_D at a fixed frequency. Figure 3D is a representative plot of S_I *versus* I_D at 10 Hz collected at V_{DS} = 1 V with V_{GS} ranging from 50 to 7.5 V (blue points) and at V_{DS} = 50 V with V_{GS} spanning from 50 to 30 V (black points). The double logarithm plot shows three distinct slopes. The inset of Figure 3D shows the statistics of the slopes measured from four devices at frequencies of 5 to 10 Hz (in steps of 1 Hz), where slopes of 1.6 ± 0.04 in the saturation regime, 1.2 ± 0.07 in the linear regime, and 2.0 ± 0.01 in the subthreshold regime are found. These experimental results closely match the Hooge model for operation in both saturation (eq 2) and linear (eq 1) regimes, suggesting that mobility fluctuations are responsible for the 1/*f* noise behavior under strong accumulation of charge. For the subthreshold regime (eq 3), 1/*f* noise is consistent with carrier number fluctuation based on the McWhorter theory. Alternatively, S_I/I_D^2 or S_I *versus* the ($V_{GS}-V_T$) relationship can be used to distinguish between Hooge and McWhorter models.[56] In Supporting Information Figure S6, both linear and saturation regimes are again shown to follow the Hooge model instead of the McWhorter model, consistent with the results from S_I *versus* I_D. Based on the McWhorter model in eq 3, the calculated N_T is ~8.17 × 10^{18} (eV^{-1} cm^{-3}), which is 1 order of magnitude lower than that found for a-Si[28] and similar to that for a-InGaZnO transistors.[51] For unencapsulated devices, the S_I *versus* I_D does not show these trends in all three operation modes, which we believe is due to bias stress effects on the measurement of I_D.

The Hooge parameter (α_H) is commonly used as a figure-of-merit to compare the 1/*f* noise level in different systems. The Hooge parameter calculated from the normalized current spectral density is $(S_I/I_D^2) = A/f = \alpha_H/N_f$, where *A* is the noise amplitude (described above) equal to the Hooge parameter divided by the carrier number $N = WLC_{ox}/q(V_{GS} - V_T)$.[24,56] Figure 4A,B and Supporting Information Figure S7A,B compare the field-effect carrier mobility and Hooge parameter as a function of V_{GS} in the saturation and linear regimes,

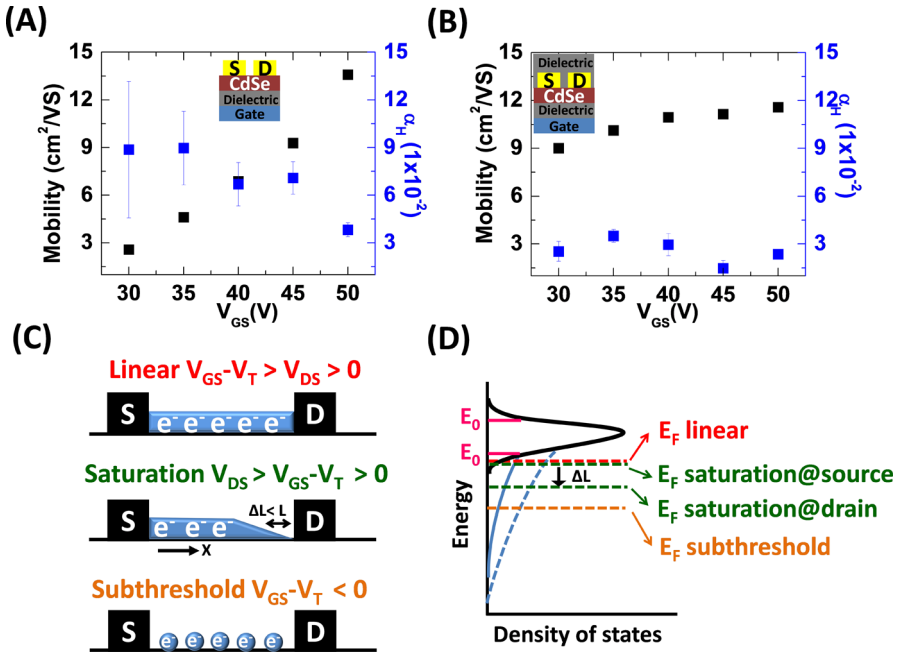

Figure 4. Mobility and Hooge parameter (α_H) as a function of V_{GS} when V_{DS} = 50 V for (A) unencapsulated, top-contact and (B) Al_2O_3-encapsulated, top-contact devices. Insets in (A) and (B) are NCFET schematics. (C) Schematic of the carrier concentration in the NCFET channel, and (D) density of states for NC thin films and the energy of the Fermi level in the linear (red), saturation (green), and subthreshold (orange) regimes. E_0 denotes the mobility edge. Note, in the saturation region, pinch off within ΔL of the drain electrode causes the Fermi energy to move further away from the band edge. The density of tail states (blue dashed) is reduced after Al_2O_3 encapsulation (blue solid).

respectively, for unencapsulated and encapsulated devices. For unencapsulated TC devices (Figure 4A and Supporting Information Figure S7A), a strong gate-dependent carrier mobility and Hooge parameter are observed, with the mobility and Hooge parameter inversely related. Encapsulated devices retain a consistently small Hooge parameter of around 3×10^{-2}, as well as a significantly weaker gate-dependent carrier mobility of around 10 cm^2/Vs. This result highlights the influences of NC surface states on device carrier mobility and noise magnitude.

On the basis of our experimental observations in Figure 3 and Figure 4A,B, we describe the 1/*f* noise mechanism by a schematic of the carrier concentration (Figure 4C) and therefore Fermi energy (E_F) across the NCFET channel, accounting for the NC thin-film density of states (Figure 4D). The density of states for strongly coupled, NC thin films is consistent with the formation of extended states above the mobility edge and tail and midgap states that extend into the gap.[9,14,57,58] Site-to-site variation even in highly monodisperse NC samples introduces dispersion in the energy of NC states that tail below the mobility edge. NCs possess a large surface-to-volume ratio, and therefore, the surface is known to play a dominant role on their physical properties, as dangling bonds, some ligand chemistries, and exposure to oxygen and water introduce electronic trap states within the band gap.[14,59,60] In the transistor geometry, we showed previously that the semiconductor NC/gate dielectric interface also contributes to the density of tail states.[9] These tail and midgap states, either from NC energy dispersion or surface states or the NC/gate dielectric interface, when not filled, have a significant influence on NC thin-film device performance, limiting carrier lifetime[61] and mobility and introducing device hysteresis and instability under bias stress.[54] For CdSe NCFETs without Al_2O_3 encapsulation, we assume a greater density of tail and midgap states from incomplete passivation and/or surface oxygen/water adsorption over time even in a nitrogen-filled glovebox (Figure 4D, blue dashed line), as previously reported for lead chalcogenide NCFETs.[62−64] During ALD Al_2O_3 growth, additional indium diffuses from the source and drain electrodes into the NC channel to better passivate the NC surfaces.[5] The deposited Al_2O_3 also encapsulates the NCs and the device interfaces, preventing oxygen and water from introducing trap states (Figure 4D, blue solid line).[5,54] The calculated CdSe NCs/Al_2O_3 interface trap density is similar for devices with and without Al_2O_3 encapsulation (Supporting Information Figure S4), consistent with the change in trap density mainly resulting from passivation of NC surface states.

In the transistor geometry, the applied V_{GS} tunes the Fermi energy (E_F) in the semiconductor channel, modulating the free carrier concentration and the occupancy of sub-band gap states. In encapsulated devices, when $V_{GS} > V_T$, E_F lies close to the mobility edge (E_0) and a large concentration of free carriers is

accumulated in extended states. Here the current fluctuations that give rise to 1/*f* noise are consistent with mobility fluctuations described by the Hooge model as seen in the linear and saturation regimes in Figure 3D. The carrier mobility and Hooge parameter are stable over a range of V_{GS} from 50 to 30 V in the saturation (Figure 4B) and linear (Supporting Information Figure S7B) regimes, in agreement with the low density of unoccupied sub-band gap states. In the linear regime ($V_{DS} < V_{GS} - V_T$), a nearly constant $\gamma = -1$ is observed as a uniform charge accumulation layer exists. Unlike the uniform E_F and carrier concentration in the linear regime, E_F in the saturation regime will gradually move away from the mobility edge as the channel is pinched off due to the reverse bias near the drain electrode (Figure 4C), leaving behind empty, deeper trap states for carriers to communicate with by trapping−detrapping. Compared to shallow traps, these unoccupied deep trap states give rise to slow carrier trapping−detrapping and therefore appear as low-frequency 1/*f* noise, consistent with the deviation from $\gamma = -1$ in the saturation regime (as smaller V_{GS} increases the width of the pinch off region as $V_{DS} > V_{GS} - V_T$ increases).[30] When $V_{GS} < V_T$ in the subthreshold regime, E_F is away from the mobility edge and gives rise to an abrupt change in γ (Figure 3C) and a transition in the 1/*f* noise from carrier mobility to number fluctuations in accordance with the McWhorter model. In contrast, in unencapsulated devices, the high density of tail states results in appreciable carrier trapping−detrapping. As seen in Figure 4A and Supporting Information Figure S7A, the mobility and Hooge parameter have a strong V_{GS} dependence in both the linear and saturation regimes, leading in saturation to a factor of 4 increase in the Hooge parameter. The relationship between increased density of sub-band gap states and increased low-frequency noise has similarly been reported in a-InGaZnO transistors.[46,65] These sub-band gap states have also been correlated with an increased Hooge parameter and bias instability. Similarly, our results suggest that unfilled sub-band gap states contribute to increased 1/*f* noise, increased bias stress effects, and lower carrier mobilities.

CONCLUSION

In summary, we report 1/*f* noise behavior at low frequencies in CdSe NCFETs and correlate the noise behavior with the nature of charge transport in CdSe NC thin films. The 1/*f* noise behavior in the saturation and linear regimes is consistent with charge transport of accumulated carriers in extended states where mobility fluctuations are caused by scattering. However, in the subthreshold regime, the 1/*f* noise behavior results from carrier number fluctuations arising from carrier trapping−detrapping from sub-band gap states introduced by NC dispersion, the NC surface, and/or the semiconductor NC/gate dielectric interface. We find that passivation of NC surface states gives rise to a consistent carrier mobility and Hooge parameter over a wide range of applied voltages. This is very important for high-density integrated circuits where inconsistent device characteristics and large noise limit their functionality.

METHODS

CdSe Synthesis. Trioctylphosphine oxide (90%), tributylphosphine (97%), and selenium shot (99.99%) are purchased from Sigma-Aldrich. Octadecylamine (90%) is purchased from Acros. Cadmium stearate is purchased from MP Biomedicals. Ammonium thiocyanate (Acros, 99.8%+) is recrystallized from anhydrous alcohol. All anhydrous solvents are purchased from Acros with the highest grade available or purged and then dried over activated alumina columns or distilled over a drying agent under nitrogen. Cadmium selenide NCs are synthesized based on a modified literature recipe.[66] A typical reaction starts with a mixture of 20 g of trioctylphosphine, 20 g of octadecylamine, and 2.10 g of cadmium stearate that are held under vacuum for 1 h at 120 °C. The mixture is then heated to 320 °C under dry nitrogen and then 10.0 mL of 1.25 M selenium in tributylphosphine solution is injected. The growth of the particles is continued at 290 °C for 15 min.

CdSe NC Ligand Exchange. The long ligands capping the as-synthesized CdSe NCs are exchanged with compact thiocyanate (SCN) ligands under dry nitrogen atmosphere.[10] Then, 1.2 mL of CdSe NCs is dispersed in hexane at an optical density of 10 cm^{-1} at the first excitonic absorption peak. Next, 0.6 mL of ammonium thiocyanate in acetone (20 mg/mL) is added to the CdSe NC dispersion and stirred at 3000 rpm for 2 min. Complete flocculation is observed within seconds. The mixture is centrifuged at 2000*g* for 1 min, and then the colorless supernatant is discarded. Next, 1.2 mL of tetrahydrofuran is added, stirred at 3000 rpm for 2 min, and centrifuged at 2000*g* for 1 min, and the colorless supernatant is discarded. Then, 1.2 mL of toluene is added, stirred at 3000 rpm for 1 min, and centrifuged at 2000*g* for 1 min, and the colorless supernatant is discarded. Finally, 0.2 mL of dimethylformamide is added to the NCs and gently agitated to form NC dispersions.

Device Fabrication. NCFETs are fabricated in bottom-gate configuration on N^+-doped silicon substrates with 250 nm of thermally grown SiO_2 that serves as the back gate and part of the gate dielectric stack. An additional 20 nm gate dielectric layer of Al_2O_3 is grown *via* atomic layer deposition (ALD), as the Al_2O_3 surface reduces the device interface trap density.[9,67] Then, 40 nm indium followed by 40 nm gold is thermally evaporated through shadow masks to define source and drain electrodes on top of the CdSe NC layer and complete top contact (TC) devices. The CdSe NC layer is deposited by spin-coating (500 rpm for 30 s, then 800 rpm for 30 s) to form uniform, randomly close-packed NC thin films. The order of metal evaporation is reversed (10 nm gold and 20 nm of indium) and deposited prior to spin-coating the CdSe NC layer to form bottom-contact (BC) devices. Two source−drain electrode designs are used. For constant $W/L = 15$, the channel length varies from 30 to 200 μm. Another design is used for devices with constant $W = 2400$, 1800, 1200, and 600 μm along with lengths varying from $W/L = 10$, 15, 20, and 25. The devices are annealed at 250 °C for 10 min to allow for the indium, introduced in the contacts, to diffuse across and dope the NC channel. For device encapsulation, a 50 nm layer of Al_2O_3 is deposited by ALD at a temperature of 150 °C. NCFET fabrication steps are carried out in

nitrogen-filled gloveboxes, with the exception of ALD growth of the Al_2O_3 in the dielectric stack, forming the device encapsulation layer.

Device Characterization and Flicker Noise Collection. FET device characteristics are collected on a 4156C (Agilent) semiconductor parameter analyzer. To collect low-frequency noise in NCFETs, two Keithley 2400 source meters, a SR570 (Stanford Research System) low noise current preamplifier and an HP 3582A spectrum analyzer, are used and connected with appropriate shared grounding and shielding to minimize external electrical interference. The Keithley 2400 is used to provide a constant voltage source while recording device current over time (in steps of 30 ms). The SR570 amplifies the input device current as output voltage, which is then connected to the HP 3582A spectrum analyzer. The amplification is selected based on the input device current. Through all measurements, 200 μA/V is applied for V_{DS} = 50 V and 2 μA/V is for V_{DS} = 1 V, where the bandwidth for both amplifications is greater than 10^4 Hz, far beyond the frequency range of interest in this 1/*f* noise study. A 0.03 to 3k Hz band-pass filter is selected on the SR570 amplifier. The spectrum analyzer measures frequencies from 5 to 260 Hz in steps of 1 Hz and takes 16 times to average for the stable output reading. All measurement are performed while devices remained in dry nitrogen-filled gloveboxes.

Conflict of Interest: The authors declare no competing financial interest.

Acknowledgment. The authors would like to thank, for primary support of this work, the NSF under Award No. PFI: AIR ENG-1312202 for NC ligand exchange, NCFET device fabrication and DC electrical and noise characterization, and measurement analysis. We thank the U.S. Department of Energy Office of Basic Energy Sciences, Division of Materials Science and Engineering, under Award No. DE-SC0002158 for NC synthesis and EDX spectroscopy.

Supporting Information Available: Equations and derivations describing field-effect mobility calculations, channel-length-dependent noise sources, and drain−source current decay under bias stress. Figures and tables showing interface trap, contact resistance, and noise source comparisons in TC and BC NCFETs; bias stress analysis of unencapsulated and encapsulated devices; voltage-dependent analysis of noise mechanism; and linear regime mobility and noise correlation in devices. This material is available free of charge *via* the Internet at http://pubs.acs.org.

REFERENCES AND NOTES

1. Bawendi, M. G.; Steigerwald, M. L.; Brus, L. E. The Quantum Mechanics of Larger Semiconductor Clusters ("Quantum Dots"). *Annu. Rev. Phys. Chem.* **1990**, *41*, 477–496.
2. Alivisatos, A. P. Semiconductor Clusters, Nanocrystals, and Quantum Dots. *Science* **1996**, *271*, 933–937.
3. Murray, C. B.; Kagan, C. R.; Bawendi, M. G. Synthesis and Characterization of Monodisperse Nanocrystals and Close-Packed Nanocrystal Assemblies. *Annu. Rev. Mater. Sci.* **2000**, *30*, 545–610.
4. Koh, W.-K.; Saudari, S. R.; Fafarman, A. T.; Kagan, C. R.; Murray, C. B. Thiocyanate-Capped PbS Nanocubes: Ambipolar Transport Enables Quantum Dot-Based Circuits on a Flexible Substrate. *Nano Lett.* **2011**, *11*, 4764–4767.
5. Choi, J.-H.; Oh, S. J.; Lai, Y.; Kim, D. K.; Zhao, T.; Fafarman, A. T.; Diroll, B. T.; Murray, C. B.; Kagan, C. R. *In Situ* Repair of High-Performance, Flexible Nanocrystal Electronics for Large-Area Fabrication and Operation in Air. *ACS Nano* **2013**, *7*, 8275–8283.
6. Loiudice, A.; Rizzo, A.; Grancini, G.; Biasiucci, M.; Belviso, M. R.; Corricelli, M.; Curri, M. L.; Striccoli, M.; Agostiano, A.; Cozzoli, P. D.; *et al.* Fabrication of Flexible All-Inorganic Nanocrystal Solar Cells by Room-Temperature Processing. *Energy Environ. Sci.* **2013**, *6*, 1565.
7. Tian, Q.; Xu, X.; Han, L.; Tang, M.; Zou, R.; Chen, Z.; Yu, M.; Yang, J.; Hu, J. Hydrophilic Cu_2ZnSnS_4 Nanocrystals for Printing Flexible, Low-Cost and Environmentally Friendly Solar Cells. *CrystEngComm* **2012**, *14*, 3847.
8. Liu, H.; Li, M.; Voznyy, O.; Hu, L.; Fu, Q.; Zhou, D.; Xia, Z.; Sargent, E. H.; Tang, J. Physically Flexible, Rapid-Response Gas Sensor Based on Colloidal Quantum Dot Solids. *Adv. Mater.* **2014**, *26*, 2718–2724.
9. Choi, J.-H.; Fafarman, A. T.; Oh, S. J.; Ko, D.-K.; Kim, D. K.; Diroll, B. T.; Muramoto, S.; Gillen, G.; Murray, C. B.; Kagan, C. R. Bandlike Transport in Strongly Coupled and Doped Quantum Dot Solids: A Route to High-Performance Thin-Film Electronics. *Nano Lett.* **2012**, *12*, 2631–2638.
10. Fafarman, A. T.; Koh, W.-K.; Diroll, B. T.; Kim, D. K.; Ko, D.-K.; Oh, S. J.; Ye, X.; Doan-Nguyen, V.; Crump, M. R.; Reifsnyder, D. C.; *et al.* Thiocyanate-Capped Nanocrystal Colloids: Vibrational Reporter of Surface Chemistry and Solution-Based Route to Enhanced Coupling in Nanocrystal Solids. *J. Am. Chem. Soc.* **2011**, *133*, 15753–15761.
11. Lee, J.-S.; Kovalenko, M. V.; Huang, J.; Chung, D. S.; Talapin, D. V. Band-like Transport, High Electron Mobility and High Photoconductivity in All-Inorganic Nanocrystal Arrays. *Nat. Nanotechnol.* **2011**, *6*, 348–352.
12. Kim, D. K.; Lai, Y.; Diroll, B. T.; Murray, C. B.; Kagan, C. R. Flexible and Low-Voltage Integrated Circuits Constructed from High-Performance Nanocrystal Transistors. *Nat. Commun.* **2012**, *3*, 1216.
13. Chuang, C. M.; Brown, P. R.; Bulović, V.; Bawendi, M. G. Improved Performance and Stability in Quantum Dot Solar Cells through Band Alignment Engineering. *Nat. Mater.* **2014**, *13*, 796–801.
14. Ip, A. H.; Thon, S. M.; Hoogland, S.; Voznyy, O.; Zhitomirsky, D.; Debnath, R.; Levina, L.; Rollny, L. R.; Carey, G. H.; Fischer, A.; *et al.* Hybrid Passivated Colloidal Quantum Dot Solids. *Nat. Nanotechnol.* **2012**, *7*, 577–582.
15. Gao, J.; Perkins, C. L.; Luther, J. M.; Hanna, M. C.; Chen, H.; Semonin, O. E.; Nozik, A. J.; Ellingson, R. J.; Beard, M. C. n-Type Transition Metal Oxide as a Hole Extraction Layer in PbS Quantum Dot Solar Cells. *Nano Lett.* **2011**, *11*, 3263–3266.
16. Keuleyan, S.; Lhuillier, E.; Brajuskovic, V.; Guyot-Sionnest, P. Mid-infrared HgTe Colloidal Quantum Dot Photodetectors. *Nat. Photonics* **2011**, *5*, 489–493.
17. Konstantatos, G.; Howard, I.; Fischer, A.; Hoogland, S.; Clifford, J.; Klem, E.; Levina, L.; Sargent, E. H. Ultrasensitive Solution-Cast Quantum Dot Photodetectors. *Nature* **2006**, *442*, 180–183.
18. Lhuillier, E.; Keuleyan, S.; Liu, H.; Guyot-Sionnest, P. Colloidal HgTe Material for Low-Cost Detection into the MWIR. *J. Electron. Mater.* **2012**, *41*, 2725–2729.
19. Ghibaudo, G. Critical MOSFETs Operation for Low Voltage/low Power IC's: Ideal Characteristics, Parameter Extraction, Electrical Noise and RTS Fluctuations. *Microelectron. Eng.* **1997**, *39*, 31–57.
20. Xu, Y.; Liu, C.; Scheideler, W.; Li, S.; Li, W.; Lin, Y.; Balestra, F.; Member, S.; Ghibaudo, G.; Tsukagoshi, K. Understanding Thickness-Dependent Charge Transport in Pentacene Transistors by Low-Frequency Noise. *IEEE Electron Device Lett.* **2013**, *34*, 1298–1300.
21. Shklovskii, B. 1/*f* Noise in Variable Range Hopping Conduction. *Phys. Rev. B* **2003**, *67*, 045201.
22. Burin, A.; Shklovskii, B.; Kozub, V.; Galperin, Y.; Vinokur, V. Many Electron Theory of 1/*f* Noise in Hopping Conductivity. *Phys. Rev. B* **2006**, *74*, 075205.
23. Liu, H.; Lhuillier, E.; Guyot-Sionnest, P. 1/*f* Noise in Semiconductor and Metal Nanocrystal Solids. *J. Appl. Phys.* **2014**, *115*, 154309.
24. Hooge, F. N. 1/*f* Noise Sources. *IEEE Trans. Electron Devices* **1994**, *41*, 1926–1935.
25. McWhorter, A. L.; Kingston, R. H. *Semiconductor Surface Physics*; University of Pennsylvania Press: Philadelphia, PA, 1957.
26. Vandamme, L. K. J.; Hooge, F. N. What Do We Certainly Know About 1/*f* Noise in MOSTs ?. *IEEE Trans. Electron Devices* **2008**, *55*, 3070–3085.
27. Van der Ziel, A. Unified Presentation of 1/*f* Noise in Electronic Devices: Fundamental 1/*f* Noise Sources. *Proc. IEEE* **1988**, *76*, 233–258.
28. Rhayem, J.; Rigaud, D.; Valenza, M.; Szydlo, N.; Lebrun, H. 1/*f* Noise Modeling in Long Channel Amorphous Silicon Thin Film Transistors. *J. Appl. Phys.* **2000**, *87*, 1983.

29. Martin, S.; Dodabalapur, A.; Bao, Z.; Crone, B.; Katz, H. E.; Li, W.; Passner, A.; Rogers, J. A. Flicker Noise Properties of Organic Thin-Film Transistors. *J. Appl. Phys.* **2000**, *87*, 3381.
30. Kang, H.; Jagannathan, L.; Subramanian, V. Measurement, Analysis, and Modeling of 1/*f* Noise in Pentacene Thin Film Transistors. *Appl. Phys. Lett.* **2011**, *99*, 062106.
31. Dimitriadis, C. A.; Farmakis, F. V.; Kamarinos, G.; Brini, J. Origin of Low-Frequency Noise in Polycrystalline Silicon Thin-Film Transistors. *J. Appl. Phys.* **2002**, *91*, 9919.
32. Rhayem, J.; Valenza, M.; Rigaud, D.; Szydlo, N.; Lebrun, H. 1/*f* Noise Investigations in Small Channel Length Amorphous Silicon Thin Film Transistors. *J. Appl. Phys.* **1998**, *83*, 3660.
33. Balandin, A.; Wang, K. L.; Cai, S.; Li, R.; Viswanathan, C. R.; Wang, E. N.; Wojtowicz, M. Investigation of Flicker Noise and Deep-Levels in GaN/AlGaN Transistors. *J. Electron. Mater.* **2000**, *29*, 297–301.
34. Rajamohanan, B.; Member, S.; Ok, I.; Mujumdar, S.; Hobbs, C.; Member, S. Correlated Flicker Noise and Hole Mobility Strained SiGe FINFETs. *IEEE Electron Device Lett.* **2012**, *33*, 1237–1239.
35. Necliudov, P. V.; Rumyantsev, S. L.; Shur, M. S.; Gundlach, D. J.; Jackson, T. N. 1/*f* Noise in Pentacene Organic Thin Film Transistors. *J. Appl. Phys.* **2000**, *88*, 5395.
36. Jurchescu, O. D.; Hamadani, B. H.; Xiong, H. D.; Park, S. K.; Subramanian, S.; Zimmerman, N. M.; Anthony, J. E.; Jackson, T. N.; Gundlach, D. J. Correlation between Microstructure, Electronic Properties and Flicker Noise in Organic Thin Film Transistors. *Appl. Phys. Lett.* **2008**, *92*, 132103.
37. Vandamme, L. K. J.; Feyaerts, R.; Trefán, G.; Detcheverry, C. 1/*f* Noise in Pentacene and Poly-thienylene Vinylene Thin Film Transistors. *J. Appl. Phys.* **2002**, *91*, 719.
38. Balandin, A. A. Low-Frequency 1/*f* Noise in Graphene Devices. *Nat. Nanotechnol.* **2013**, *8*, 549–555.
39. Lin, Y.-M.; Avouris, P. Strong Suppression of Electrical Noise in Bilayer Graphene Nanodevices. *Nano Lett.* **2008**, *8*, 2119–2125.
40. Grandchamp, B.; Frégonèse, S.; Majek, C.; Hainaut, C.; Maneux, C.; Meng, N.; Happy, H.; Zimmer, T. Characterization and Modeling of Graphene Transistor Low-Frequency Noise. *IEEE Trans. Electron Devices* **2012**, *59*, 516–519.
41. Lin, Y.-M.; Appenzeller, J.; Chen, Z.; Avouris, P. Electrical Transport and Noise in Semiconducting Carbon Nanotubes. *Phys. E (Amsterdam, Neth.)* **2007**, *37*, 72–77.
42. Appenzeller, J.; Lin, Y.-M.; Knoch, J.; Chen, Z.; Avouris, P. 1/*f* Noise in Carbon Nanotube Devices—On the Impact of Contacts and Device Geometry. *IEEE Trans. Nanotechnol.* **2007**, *6*, 368–373.
43. Wang, W.; Xiong, H. D.; Edelstein, M. D.; Gundlach, D.; Suehle, J. S.; Richter, C. A.; Hong, W.-K.; Lee, T. Low Frequency Noise Characterizations of ZnO Nanowire Field Effect Transistors. *J. Appl. Phys.* **2007**, *101*, 044313.
44. Kim, S.; Carpenter, P. D.; Jean, R. K.; Chen, H.; Zhou, C.; Ju, S.; Janes, D. B. Role of Self-Assembled Monolayer Passivation in Electrical Transport Properties and Flicker Noise of Nanowire Transistors. *ACS Nano* **2012**, *6*, 7352–7361.
45. Deen, M. J.; Rumyantsev, S. L.; Landheer, D.; Xu, D.-X. Low-Frequency Noise in Cadmium-Selenide Thin-Film Transistors. *Appl. Phys. Lett.* **2000**, *77*, 2234.
46. Kim, S.; Jeon, Y.; Lee, J.-H.; Ahn, B. D.; Park, S. Y.; Park, J.-H.; Kim, J. H.; Park, J.; Kim, D. M.; Kim, D. H. Relation between Low-Frequency Noise and Subgap Density of States in Amorphous InGaZnO Thin-Film Transistors. *IEEE Electron Device Lett.* **2010**, *31*, 1236–1238.
47. Sze, S. M.; Kwok, K. *Physics of Semiconductor Devices*, 3rd ed.; John Wiley & Sons: New York, 2007.
48. Fung, T.-C.; Baek, G.; Kanicki, J. Low Frequency Noise in Long Channel Amorphous In–Ga–Zn–O Thin Film Transistors. *J. Appl. Phys.* **2010**, *108*, 074518.
49. Peransin, J.; Vignaud, P.; Rigaud, D.; Vandamme, L. K. J. 1/*f* Noise in MODFET's at Low Drain Bias. *IEEE Trans. Electron Devices* **1990**, *37*, 2250–2253.
50. Lee, B.; Chen, Y.; Fu, D.; Yi, H. T.; Czelen, K.; Najafov, H.; Podzorov, V. Trap Healing and Ultralow-Noise Hall Effect at the Surface of Organic Semiconductors. *Nat. Mater.* **2013**, *12*, 1125–1129.
51. Park, J. C.; Kim, S. W.; Kim, C. J.; Kim, S.; Kim, D. H.; Cho, I.-T.; Kwon, H.-I. Low-Frequency Noise in Amorphous Indium–Gallium–Zinc Oxide Thin-Film Transistors from Subthreshold to Saturation. *Appl. Phys. Lett.* **2010**, *97*, 122104.
52. Street, R. A. Thin-Film Transistors. *Adv. Mater.* **2009**, *21*, 2007–2022.
53. Ryu, K. K.; Member, S.; Nausieda, I.; He, D. D.; Akinwande, A. I.; Bulovic, V.; Sodini, C. G. Bias-Stress Effect in Pentacene Organic Thin-Film Transistors. *IEEE Trans. Electron Devices* **2010**, *57*, 1003–1008.
54. Liu, Y.; Tolentino, J.; Gibbs, M.; Ihly, R.; Perkins, C. L.; Liu, Y.; Crawford, N. R. M.; Hemminger, J. C.; Law, M. PbSe Quantum Dot Field-Effect Transistors with Air-Stable Electron Mobilities above 7 $cm^2 V^{-1} s^{-1}$. *Nano Lett.* **2013**, *13*, 1578–1587.
55. Christensson, S.; Svensson, C. Low Frequency Noise in MOS Transistors—1 Theory. *Solid. State. Electron.* **1968**, *11*, 797–812.
56. Rigaud, D.; Valenza, M.; Rhayem, J. Low Frequency Noise in Thin Film Transistors. *IEE Proc. Circuits, Devices Syst.* **2002**, *149*, 75–82.
57. Underwood, D. F.; Kippeny, T.; Rosenthal, S. J. Ultrafast Carrier Dynamics in CdSe Nanocrystals Determined by Femtosecond Fluorescence Upconversion Spectroscopy. *J. Phys. Chem. B* **2001**, *105*, 436–443.
58. Nagpal, P.; Klimov, V. I. Role of Mid-gap States in Charge Transport and Photoconductivity in Semiconductor Nanocrystal Films. *Nat. Commun.* **2011**, *2*, 486.
59. Bozyigit, D.; Volk, S.; Yarema, O.; Wood, V. Quantification of Deep Traps in Nanocrystal Solids, Their Electronic Properties, and Their Influence on Device Behavior. *Nano Lett.* **2013**, *13*, 5284.
60. Voznyy, O. Mobile Surface Traps in CdSe Nanocrystals with Carboxylic Acid Ligands. *J. Phys. Chem. C* **2011**, *115*, 15927–15932.
61. Jeong, K. S.; Tang, J.; Liu, H.; Kim, J.; Schaefer, A. W.; Kemp, K.; Levina, L.; Wang, X.; Hoogland, S.; Debnath, R.; *et al.* Enhanced Mobility-Lifetime Products in PbS Colloidal Quantum Dot Photovoltaics. *ACS Nano* **2012**, *6*, 89–99.
62. Oh, S. J.; Kim, D. K.; Kagan, C. R. Remote Doping and Schottky Barrier Formation in Strongly Quantum Confined Single PbSe Nanowire Field-Effect Transistors. *ACS Nano* **2012**, *6*, 4328–4334.
63. Leschkies, K. S.; Kang, M. S.; Aydil, E. S.; Norris, D. J. Influence of Atmospheric Gases on the Electrical Properties of PbSe Quantum-Dot Films. *J. Phys. Chem. C* **2010**, *525*, 9988–9996.
64. Kim, D. K.; Vemulkar, T. R.; Oh, S. J.; Koh, W.; Murray, C. B.; Kagan, C. R. Ambipolar and Unipolar PbSe Nanowire Field-Effect Transistors. *ACS Nano* **2011**, *5*, 3230–3236.
65. Jeong, C.-Y.; Park, I.-J.; Cho, I.-T.; Lee, J.-H.; Cho, E.-S.; Ryu, M. K.; Park, S.-H. K.; Song, S.-H.; Kwon, H.-I. Investigation of the Low-Frequency Noise Behavior and Its Correlation with the Subgap Density of States and Bias-Induced Instabilities in Amorphous InGaZnO Thin-Film Transistors with Various Oxygen Flow Rates. *Jpn. J. Appl. Phys.* **2012**, *51*, 100206.
66. Qu, L.; Peng, X. Control of Photoluminescence Properties of CdSe Nanocrystals in Growth. *J. Am. Chem. Soc.* **2002**, *124*, 2049–2055.
67. Kim, D. K.; Lai, Y.; Vemulkar, T. R.; Kagan, C. R. Flexible, Low-Voltage, and Low-Hysteresis PbSe Nanowire Field-Effect Transistors. *ACS Nano* **2011**, 10074–10083.